



JGR Solid Earth



RESEARCH ARTICLE

10.1029/2020JB021281

Key Points:

- · The reason why velocity increases with increasing viscosity is given
- A clever numerical method used to study the influence of viscosity diffusion on justifying weak or strong field geodynamo process
- The direct scaling law between a certain physical parameter, viscosity, with velocity and magnetic field of the outer core

Correspondence to:

H. Zhang, hzhang@ucas.ac.cn

Citation:

Dong, C., Zhang, H., Jiao, L., Cheng, H., Yuen, D. A., & Shi, Y. (2021). The non-negligible effect of viscosity diffusion on the geodynamo process. Journal of Geophysical Research: Solid Earth, 126, e2020JB021281. https://doi. org/10.1029/2020JB021281

Received 3 NOV 2020 Accepted 11 MAY 2021

The Non-Negligible Effect of Viscosity Diffusion on the **Geodynamo Process**

Chao Dong¹, Huai Zhang^{2,3}, Liguo Jiao¹, Huihong Cheng², David A Yuen⁴, and Yaolin Shi²



¹Institute of Geophysics, Chinese Earthquake Administration, Beijing, China, ²Key Laboratory of Computational Geodynamics, University of Chinese Academy of Sciences, Beijing, China, ³Laboratory for Marine Mineral Resources, Qingdao National Laboratory for Marine Science and Technology, Qingdao, China, ⁴Department of Earth Sciences, University of Minnesota, Minneapolis, MN, USA

Abstract Exploring geodynamo's scaling laws is of great importance when a tremendous gap still lies between realistic physics and estimated model parameters. Existing scaling laws need to be tested by numerical simulations. To boost these, taking the outer core viscosity ν , we studied its impacts on weak and strong field geodynamo outputs by varying ν in two orders of magnitudes. In the weak field mode, the fluid velocity u varies with v by a scaling law of $u \sim v^{0.52}$. While in the strong field mode, u varies very slowly by a scaling law of $u \sim v^{0.10}$. The magnetic field B does not change much with ν when the driving force is not too strong ($R_a = 12,000$) but decreases with ν by a scaling law of $B \sim \nu^{-0.20}$ when geodynamo operates in a very vigorous mode ($R_a = 50,000$). The reason that u increases with v is essential that increasing v breaks the Taylor-Proudman constraint and drops the critical Rayleigh number, but this kind of increase of u does not give a stronger B. Furthermore, we conducted a local force balance analysis and demonstrated that the balance shifts under different ν . In a quasi-MAC regime, the Lorentz force instead of the inertial force enters into the first-order agostrophic force balance, though the viscous force still plays a role. Comparing with other scaling laws previous wisdom holds, we propose that the effect of viscosity diffusion is non-negligible for both existing weak and strong dynamo regimes. Still, appropriate assumptions can be made to take this variation into account.

1. Introduction

Paleomagnetic records indicate that the Earth's geomagnetic field has existed for at least 3 billion years, with a roughly reversal rate of hundreds of thousands of years. Earth's magnetic field is generated and maintained by a strongly coupled mechanism known as geodynamo (Roberts, 2007). As emerging from numerical simulations, details of these mechanisms achieve a self-sustaining magnetic field (Aubert, 2020; Buffett, 2000; Yadav et al., 2015). From 1950 to 1990, the dynamo theory has shown that the principle of a homogeneous dynamo process is possible and has elucidated the parameter prerequisites and model constraints. In 1995, there was a breakthrough in the numerical simulation of magnetohydrodynamic (MHD) flow by Glatzmaiers and Roberts, called GR95 (Glatzmaiers & Roberts, 1995b). The GR95 model showed that such models could describe and explain many basic properties of the geomagnetic field, including dipole-dominated morphology, reversals, and westward drift (Glatzmaiers & Roberts, 1995a).

Furthermore, they studied viscous and electromagnetic coupling between the inner core and the outer core, which brought differential rotation of the inner core (Glatzmaiers & Roberts, 1995a). A couple of years later, numerous numerical geodynamo models emerged, for a comprehensive review see Christensen and Wicht (2007). For those models, the magnetic field properties closely match the geomagnetic field in terms of spatial spectra and magnetic field morphology, secular variation, and occasionally the characteristics of dipole reversals (Aubert, 2020; Calkins et al., 2017; Wicht & Sanchez, 2019; Yadav et al., 2016).

Nevertheless, the huge gap between the simulations' parameter and their expected values in the Earth's core still exists (Aubert, 2018; Schaeffer et al., 2017; Schwaiger et al., 2019). Most models have four critical dimensionless parameters: the Rayleigh number R_a , measures thermal driven force; the Ekman number E, measures the relative importance of viscous forces to Coriolis forces; the Prandtl number P_r , measures the ratio of viscosity to thermal diffusivity; and the magnetic Prandtl number P_m , measures the ratio of viscosity to magnetic diffusivity (Christensen et al., 1999). Among the unsolved issues, the value space of controlling

© 2021. The Authors. This is an open access article under the terms of the Creative Commons Attribution License, which permits use, distribution and reproduction in any medium, provided the original work is properly cited.

DONG ET AL. 1 of 19



parameters, such as the Ekman number and the magnetic Prandtl number, differs dramatically from the realistic planetary parameters (Christensen & Aubert, 2006).

Numerical geodynamo simulations require massive parallel computers than currently available to solve the rapid rotation against the outer core's low viscosity (corresponding to the low value of E). Physically, E is estimated as small as 10^{-15} . However, nowadays, geodynamo simulations have only been capable of operating down to 10^{-8} in practice (Aubert et al., 2017). A huge gap cannot be captured by limited supercomputing capacity. For instance, Christopher et al. (2010) showed that even $E=10^{-9}$ would require at least 13,000 days to calculate one single magnetic diffusion time on a 54,000-processor supercomputer, a formidable computational challenge from both the numerically stable schemes and reliable parallel solvers of the ill-conditioned linear system arising from the multiscale intrinsic nature of the geodynamo mechanism. More importantly, more recent investigations pointed out the sensitivity of these model parameters to the Earthlike dynamo simulation (Aubert, 2019; Wicht & Sanchez, 2019). Therefore, these parameters' effects on the dynamo system, such as the relationship between parameter variations and their impacts on the magnetic field generated, the sustainable velocity field, and temperature perturbations, are of significant importance.

So, the fundamental purpose of second-generation geodynamo models is to explore the parameter space and derived scaling laws (Aubert, 2020; Christensen & Aubert, 2006; Schaeffer et al., 2017). Previous studies have shown promising results with regards to this problem, for example, by analyzing the effects of one single parameter: R_a (Aubert et al., 2017; Davidson, 2013; Kuang et al., 2008; Olson et al., 1999; Sreenivasan et al., 2014; Wang et al., 2013), E (Kuang et al., 2017; Sarson et al., 1998), and P_m (Calkins et al., 2017; Christensen & Aubert, 2006; Schaeffer et al., 2017; Simitev & Busse, 2005), or by performing comprehensive study in parameter space (Christensen & Aubert, 2006; Christensen et al., 1999; Davidson, 2013; Gillet & Jones, 2006; Jones, 2011). Many scaling laws and quantitative conclusions have thus been derived. Jones (2011) investigated in which parameter space does the geodynamo behaves as dipole-dominated or multipole-dominated. Starchenko and Jones (2002) discovered how to estimate the strength of the flow and the magnetic field from a given parameter. Christensen and Aubert (2006) studied whether the magnetic field's power was related to various diffusion coefficients. However, the four major dimensionless parameters mentioned above usually depend on all of the physical coefficients for different geodynamo models. Thus, their variations are not self-dependable, which leads to the doubt on the applicability of existing conclusions. Besides, some scaling laws related to additional dimensionless parameters which make the scaling rules more physically complex. It is significantly difficult to understand the physical mechanisms behind them.

A majority of works about Earth's core's viscosity focus on the effects on the geodynamo process. Sarson et al. (1998) studied the impact of the variation of *E* on the dynamo and found that both the magnetic and the flow field are concentrated near the ICB. Soderlund et al. (2012) highlighted the significant role of viscosity in their numerical simulation. Magnetic forces did not seem to play a major role, contrary to what is expected for the real Earth. King and Buffett (2013) confirmed the non-negligible of viscosity diffusion in their simulation. Cheng and Aurnou (2016) showed that the diffusionless scaling laws were hiding an actual dependency upon viscosity. Oruba and Dormy (2014) derived alternative scaling statutes in which the magnetic field intensity depends upon viscosity and rotation rate. In conclusion, viscosity plays a significant role in the geodynamo process. However, previous studies do not directly determine the quantitative impact of viscosity, nor does it provide an intuitive physical mechanism.

To investigate the effects of viscosity on the geodynamo mechanism and deduce the output when the estimated numerical model parameters are close to the physical parameters, we adopt the Modular, Scalable, Self-consistent, and Three-dimensional (MoSST) model and conduct numerical experiments to address these issues. MoSST model has been developed from the KB97 model (Kuang & Bloxham, 1997). In addition to some improvements in the numerical schemes, it also includes some additional functional modules/features. In most of the numerical geodynamo models in practice, the viscous diffusion time is introduced as a typical timescale. While in the MoSST model, the magnetic diffusion time is used. Of all the dimensionless parameters, only the Ekman number contains the viscous term. Therefore, the advantage of using MoSST model to study the influence of viscosity is that changing E can be directly equivalent to change ν , without

DONG ET AL. 2 of 19



involving the covariant changes of other model parameters. Those uncertainties thus are avoided, and more reliable conclusions are expected.

This study is structured as follows: The MoSST model is introduced in the Section 2. In the Section 3, we study the effects of viscosity on fields and the length scale in the outer core and analyze the system's force balance. In the Section 4, the physical mechanisms behind the geodynamo model are investigated. Finally, the summary and discussions are delivered in Section 5.

2. The MoSST Model

The geodynamo model's governing equations in the spherical coordinates are composed of the momentum equation (Navier-Stokes equation), the magnetic induction equation, the energy equation (conduction/diffusion equation of thermal field), and the nondivergent constraints of both the velocity and magnetic fields. Under the Boussinesq approximation, dimensionless forms of the above equations are (Kuang & Bloxham, 1997)

$$R_{o}\left(\partial_{t} + \mathbf{u} \cdot \nabla\right)\mathbf{u} + \mathbf{1}_{z} \times \mathbf{u} = -\nabla P + \nabla \times \mathbf{B} \times \mathbf{B} + E\nabla^{2}\mathbf{u} + R_{a}\Theta\mathbf{r}$$

$$\left(\partial_{t} - \nabla^{2}\right)\mathbf{B} = \nabla \times \left(\mathbf{u} \times \mathbf{B}\right)$$

$$\left(\partial_{t} - q_{\kappa}\nabla^{2}\right)\Theta = -\mathbf{u} \cdot \nabla\left[T_{0}(r) + \Theta\right]$$

$$\nabla \cdot \mathbf{u} = 0$$

$$\nabla \cdot \mathbf{B} = 0.$$
(1)

where R_o is the magnetic Rossby number, \mathbf{u} is the flow velocity in the outer core, P is the pressure after the correction, \mathbf{B} is the magnetic induction intensity, E is the Ekman number, R_a is the Rayleigh number, Θ is the temperature perturbation, r is the radius, q_{κ} is the modified Prandtl number, and T_0 is the conducting background state (u = B = 0).

The dimensionless parameters in Equation 1 are defined as:

$$R_o = \frac{\eta}{2\Omega r_o^2}, E = \frac{v}{2\Omega r_o^2}, R_a = \frac{\alpha h_T r_o^2 g}{2\Omega \eta}, q_K = \frac{\kappa}{\eta}, \tag{2}$$

which η is the magnetic diffusion, Ω is the angular velocity, r_o is the radius of the outer core, ν is the kinematic viscosity, α is the thermal expansion coefficient in the outer core, h_T is the temperature gradient at ICB, g is gravitational acceleration, and κ is the thermal diffusivity.

It is worthwhile to mention that, of the four parameters in Equation 2, ν appears only in the definition of E, which is significantly different from the dimensionless description of other models (Kono & Roberts, 2002). Therefore, this dynamo parameter definition allows easy isolation of the viscous effect by changing only the Ekman number. Meanwhile, taking magnetic diffusion time $\tau^* = r_o^2 / \eta$ as the typical time scale is direct and appropriate. Other nondimensional scales are: $u^* = \eta / r_o$, $B^* = \sqrt{2\Omega\mu\rho\eta}$, $T^* = h_T r_o$ (Kuang & Bloxham, 1999).

The boundary conditions chosen in our numerical simulation model are as follows: The velocity field at ICB and CMB is free-slip, which holds for $\mathbf{1}_n \cdot \mathbf{u} = \mathbf{1}_n \times \left(\boldsymbol{\sigma}_v \cdot \mathbf{1}_n \right) = 0$, where $\mathbf{1}_n$ is the normal vector of the boundaries, and $\boldsymbol{\sigma}_v$ is the viscous stress tensor. The magnetic field at ICB and CMB obeys the finite electrically conducting boundary condition as $\begin{bmatrix} \mathbf{B} \end{bmatrix} = \begin{bmatrix} \mathbf{1}_n \times \mathbf{F} \end{bmatrix} = \begin{bmatrix} \mathbf{1}_n \times \mathbf{F} \end{bmatrix} = 0$, where $\begin{bmatrix} \mathbf{I} \end{bmatrix}$ denotes the difference across the boundaries, \mathbf{E} is the dimensionless electrical field. A D" layer with 1 / 10 conductivity of the CMB is included outside the CMB. Fixed heat flux boundary condition $\partial \theta / \partial r = 0$, at both ICB and CMB, is adopted for the temperature field. The initial state of our model is derived from previous simulation results.

The MoSST model is discretized by the fourth-order compact finite difference scheme in the radial direction, using zero points of Chebyshev polynomial expansion as the radial mesh configuration nodes. The number of nodes is 35, 39 and 19 for the inner core, outer core, and D" layer, respectively. On the spherical

DONG ET AL. 3 of 19

Table 1 Definitions of Dimensionless Parameters in MoSST						
Name (Symbol)	Definition	Physical significance	Core	Simulations		
Magnetic Rossby (R_o)	$rac{\eta}{2\Omega r_o^2}$	The ratio between inertial forces and Coriolis forces	10 ⁻⁹	1.25×10^{-6}		
Ekman (E)	$rac{ u}{2\Omega r_o^2}$	The ratio between viscous and Coriolis forces	10^{-15}	$6 \times 10^{-7} \sim 5 \times 10^{-5}$		
Rayleigh (R_a)	$rac{lpha h_T r_o^2 g}{2\Omega \eta}$	Thermal driven force	*	$1.2 \times 10^4 \sim 5 \times 10^4$		
Magnetic Prandtl (q_{κ})	$\frac{\kappa}{\eta}$	The ratio of thermal diffusivity to magnetic diffusivity	10^{-6}	1		

^{*}Leaving R_a blank here because the super adiabatic heat flow (or, more generally, the buoyancy flux) is not well constrained for the Earth's core yet. MoSST, Modular, Scalable, Self-consistent, and Three-dimensional.

surface (horizontal direction), spherical harmonic expansion and the pseudospectral method are adopted, and fast spectral transform (FFT) is performed. The truncation order of spherical harmonic expansion is $l_{\rm max}=33, m_{\rm max}=21.$ According to the truncation orders, the number of spherical direction nodes is 50 at θ direction and 64 at φ direction. The total number of meshes in the simulation is 277,830.

To avoid high truncation for the initial transient period and to reduce the CPU time for the process, hyperdiffusion for viscosity ν is introduced by (Kuang & Bloxham, 1999):

$$v = v_0 \left[1 + \alpha(l) \right], \alpha(l) = \begin{cases} 0, & \text{for } l \le l_0, \\ \epsilon(l - l_0)^2, & \text{for } l > l_0, \end{cases}$$
(3)

where v_0 is the original viscosity, ϵ is an artificially selected small number, l is the spherical harmonic order, and l_0 is an artificially selected spherical harmonic order. Similarly, thermal hyperdiffusion and magnetic hyperdiffusion are also introduced. This approach was first introduced by Glatzmaiers and Roberts (1995a), who obtained the first three-dimensional self-consistent dynamo model of GR95. The hyperdiffusion scheme of Equation 3 is a relatively weaker form than GR95. We choose $l_0=4$, $\epsilon=0.05$ in our simulation. The impacts of hyperdiffusion on our scaling laws will be discussed in Section 4.4.

3. Numerical Simulation Results

Dimensionless parameters control numerical simulation results. The MoSST model has four dimensionless parameters: R_o , E, R_a , and q_κ . The details are shown in Table 1. The outer core values estimated in Table 1 are calculated from the physical parameters estimated by Olson (2007) and Christensen and Wicht (2007). The four parameters indicate a large gap between the numerical model and the realistic Earth. Unfortunately, a high-performance parallel machine's current computing power is far below the capacity required to reach Earth parameter values. So far, significant efforts have to be made in the future.

3.1. Diagnostic Outputs

Since the governing equations are strongly nonlinear systems with highly coupled physical fields, huge iteration steps are needed to reach a stable electromagnetism output state after the initial state is input. To determine whether the system has been self-evolved to this state, we rely on the diagnostic outputs. An example of the diagnostic output plot is shown in Figure 1, with the horizontal coordinate as the magnetic free decay time, measured by the free diffusion time as $\tau_f = r_o^2 / \pi^2 \eta$ ($r_o = 3.5 \times 10^6 \,$ m, $\eta = 1 \,$ m $^2 / s$, $\tau_f \approx 4 \times 10^4 \,$ yr). The vertical ordinates of Figures 1a–1f show the velocity field (u), the magnetic field (B), and the temperature

DONG ET AL. 4 of 19



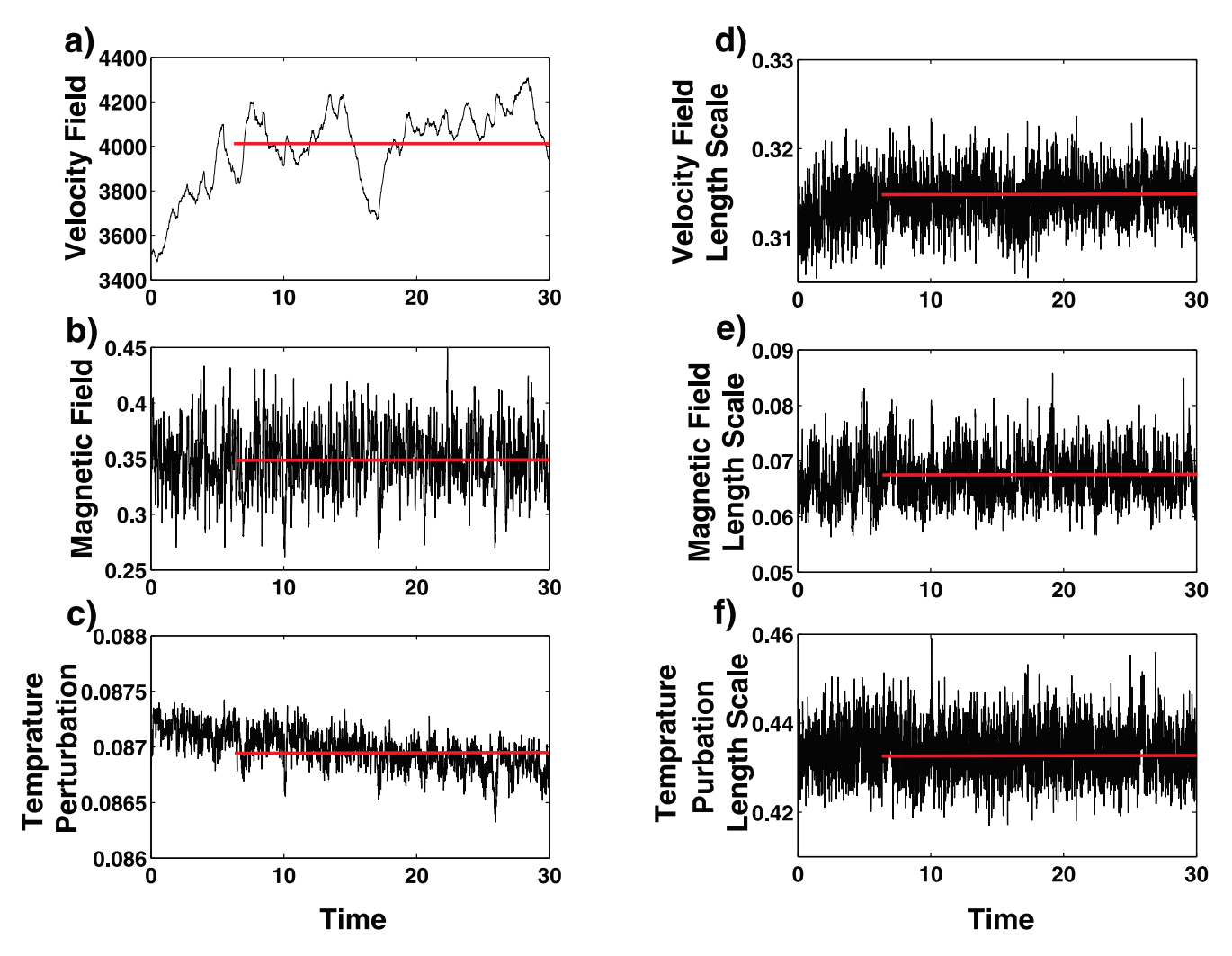


Figure 1. The diagnostic output of the MoSST model. All the panels' values are the RMS of the calculated physical values in the entire outer core. As an example, the outer core flow velocity is defined as $u = \left\|u_{\text{outer core}}\right\|_2 = \sqrt{u_1^2 + u_2^2 + \dots + u_N^2}$, and the typical scale is also the RMS result, calculated by $l_u = \left\|u/\omega\right\|_2 = \left\|u/\nabla \times u\right\|_2$. MoSST, Modular, Scalable, Self-consistent, and Three-dimensional.

perturbation (Θ), respectively. The typical spatial scales are corresponding to the three physical fields, velocity field length scale (l_u), magnetic field length scale (l_B), and temperature perturbation length scale (l_{Θ}).

With these definitions, we estimate the stable output basing on the fact that all physical quantities and their typical scales have been stabilized for at least one τ_f . The final result is an average over the stable period, as indicated by the red line in Figure 1. The transient time depends on the parameter selection, boundary conditions, initial state, and hyper diffusion scheme. As limited by the computing capacity, in general, it takes 4–5 days to obtain a stable output. For some extreme cases, it may need 2 weeks or more to receive one sound output.

3.2. Variations of Physical Fields With Ekman Number

By changing the dimensionless parameter E when $R_a=12,000$, a series of stable output results are obtained, as shown in Table 2. According to the former study of Kuang and Bloxham (1999), the R_a here is first selected between R_a^m (the threshold of R_a for dynamo action occurs, $R_a^m \sim 6,300$ for $E=10^{-5}$) and R_a^S (the threshold of R_a for strong dynamo occurs, $R_a^S \sim 13,000$ for $E=2\times 10^{-5}$). It should be mentioned that since we use a different $R_o=1.25\times 10^{-6}$, which is smaller than that of Kuang and Bloxham (1999) by one order

DONG ET AL. 5 of 19



Table 2Output Results With Different Values of Ekman Number When $R_a = 12,000$

Ekman	и	В	Θ	l_u	l_B	l_{Θ}
6.00E-07	839.4	0.3684	0.0779	0.1508	0.0663	0.4830
8.00E-07	1002.2	0.3768	0.0791	0.1742	0.0657	0.4760
1.00E-06	1154.8	0.3863	0.0812	0.1932	0.0657	0.4755
1.25E-06	1294.0	0.3883	0.0807	0.2109	0.0660	0.4622
2.00E-06	1584.9	0.3847	0.0841	0.2429	0.0645	0.4642
2.50E-06	1679.0	0.3826	0.0841	0.2530	0.0640	0.4563
4.00E-06	2023.7	0.3759	0.0861	0.2769	0.0647	0.4524
5.00E-06	2348.0	0.3706	0.0865	0.2900	0.0649	0.4481
6.00E-06	2620.4	0.3694	0.0866	0.2979	0.0653	0.4436
8.00E-06	3199.5	0.3585	0.0870	0.3082	0.0664	0.4391
1.00E-05	4060.8	0.3498	0.0870	0.3150	0.0672	0.4336
1.25E-05	4450.0	0.3397	0.0877	0.3172	0.0683	0.4328
2.00E-05	6059.9	0.3018	0.0874	0.3206	0.0698	0.4219
2.50E-05	7540.0	0.3092	0.0883	0.3215	0.0689	0.4218
5.00E-05	8332.0	0.3794	0.0893	0.3212	0.0653	0.4095

and more close to the real value in Earth's core (10^{-9}) , R_a^m , R_a^S and the following force balance may be different with those of Kuang and Bloxham (1999). Since the geodynamo system operates at a very nonlinear state, and the initial condition may affect the final results, we have selected the suitable outputs and get rid of the singular data set when searching for and analyzing the regularity. As shown in Table 2, the flow velocity uincreases significantly with E, and its amplitude varies by more than one order. Similarly, the temperature perturbation Θ increases monotonically with E, but the change is very small ($\sim 6\%$), suggesting that even a tiny temperature perturbation can lead to a significant increase in flow velocity. By contrast, the magnetic field B changes nonmonotonically with E, and it appears a trend of up first (from $E = 6 \times 10^{-7}$ to 1.25×10^{-6}), then down (to 1.25×10^{-5}) and up again (to 5×10^{-5}). The variation in the selected range is not significant, and the maximum does not exceed 30%. The results also show that a substantial increase in flow velocity does not necessarily result in considerable magnetic field growth.

In Table 2, we also list the typical spatial scales of the physical fields. As can be seen, l_u increases monotonically with E by a variation of 53%. For the typical length scale of B, l_B does not change monotonically with E. l_B does not change much, and its variation is as small as \sim 8%. In contrast to the Θ variation, the temperature perturbation length scale l_{Θ} decreases monotonically with E, and the amplitude is less than 16%.

In our model, we take $r_o = 3,500$ km and $r_i = 1,200$ km, so the flow field's typical scale is equivalent to 2–3 wavelengths in the outer core. From our

numerical results, there are \sim 10 wavelengths of the magnetic field in the outer core, and the scale is \sim 1/3–1/5 of the flow field. The temperature perturbation is about half the wavelengths in the outer core, larger than the convection's typical scale. The specific scales of these three physical fields are all shown to be typically in large scales. The spatial scale of the temperature perturbation is larger than the scale of convection, and the scale of convection is larger than the scale of the magnetic field. These may reflect the fact that the temperature perturbation motivates convection, and convection motivates the magnetic field. Details of these dynamics at different scales, and the stacking of energy at various scales, can be found in the work of Huguet and Amit (2012) and Calkins et al. (2015).

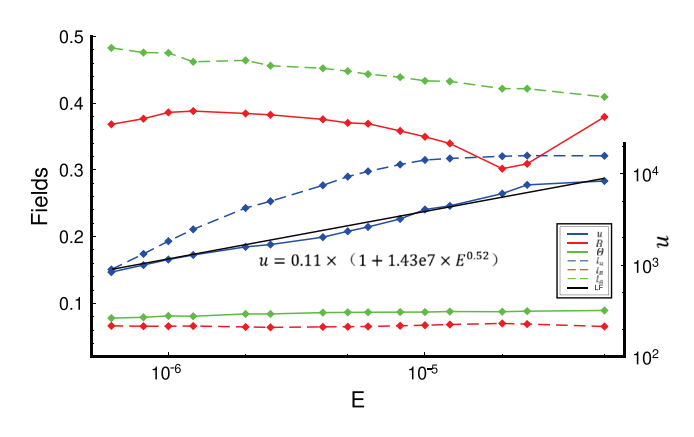


Figure 2. Variations in physical fields and their typical length scales with different values of Ekman number when $R_a=12,000$. Solid lines represent the physical fields, dashed lines are the corresponding typical scales, and different colors represent different physical fields, as shown in the legend. The black line is the result of the linear fitting (LF) of velocity changes.

Figure 2 illustrates the data in Table 2. It is clear that the influence of viscosity on the geodynamo occurs mainly in the flow field: the higher the viscosity, the more vigorous the convection. For quantitative studies, former scaling relations fitted the numerical results with power laws, such as $f = E^{\alpha}$ (Christensen & Aubert, 2006; King & Buffett, 2013). In this form, both fields and their typical length scales would vanish in the inviscid limit (E = 0). Thus, here we assume a different scaling law of the form:

$$f = f_0 \Big(1 + \alpha E^{\beta} \Big), \tag{4}$$

where f_0 is the independent of E, and represents its inviscid limit. Then the least square fit is used to estimate the three parameters f_0 , α , and β .

By applying Equation 4 to the velocity field u and its typical length scale l_u , we have

$$u = 0.11 \times (1 + 1.43e7 \times E^{0.52}) (\text{or } u = 0.11 \times (1 + 1.43e7 \times v^{0.52})),$$
 (5)

DONG ET AL. 6 of 19

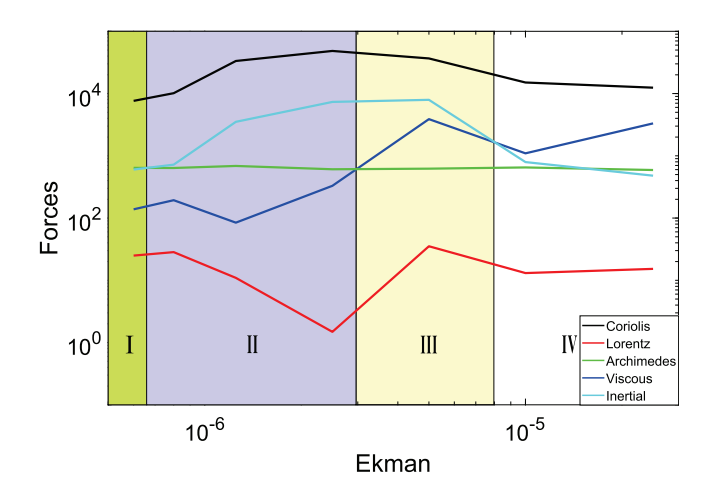


Figure 3. Force balance with different values of Ekman number when $R_a = 12,000$. Different colors represent different forces, as shown in the legend.

$$l_u = 0.01 \times \left(1 + 84.32 \times E^{0.12}\right),\tag{6}$$

as for the magnetic field, we will have

$$B = 0.05 \times \left(1 + 4.32 \times E^{-0.04}\right). \tag{7}$$

3.3. Force Balance

The fluid motion in the outer core is affected by various forces. And the force equilibrium mechanisms determine the dynamics in the outer core. In this part, we analyze details of the force balance under different viscosities. The momentum equation in Equation 1 gives

$$\underbrace{R_o\left(\hat{o}_t + \mathbf{u} \cdot \nabla\right)\mathbf{u}}_{\text{Inertia}} + \underbrace{1_z \times \mathbf{u}}_{\text{Coriolis}} = \underbrace{-\nabla P}_{\text{pressure}} + \underbrace{\nabla \times \mathbf{B} \times \mathbf{B}}_{\text{Lorentz}} + \underbrace{E\nabla^2 \mathbf{u}}_{\text{viscous}} + \underbrace{R_a \Theta \mathbf{r}}_{\text{buoyancy}}. \tag{8}$$

Equation 8 includes five forces: inertial force F_I , Coriolis force F_C , pressures gradient F_P , Lorentz force F_L , viscous force F_V , and thermal buoyancy F_A (Archimedes force).

Among them, the leading-order force balance is between F_C and F_P , with the remaining puny part compensated by others, which is called the quasi-geostrophic (QG) state (Schwaiger et al., 2019). If F_L is close to F_C and far beyond other forces (F_A , F_I , and F_V), this will be called the magneto-quasi-geostrophic state, in that the uncompensated part of F_C + F_P (also called the ageostrophic Coriolis) is mainly balanced by F_L at zeroth order. Traditionally, geodynamo is assumed to operate on a QG-MAC state (shorted for MAC), in which the ageostrophic F_C is balanced by F_A + F_L at first order. A MAC balance is usually treated as equal to the so-called strong field dynamo, while a discrepancy exists between the two definitions. In strong field dynamos, the ratio between F_L and F_C defined as the Elsasser number (in dimensional form) is

$$\Lambda = \frac{F_L}{F_C} = \frac{B^2}{\Omega\mu\rho\eta},\tag{9}$$

is of O(1). A MAC state is somewhat different from a strong field in that the Λ of the former could be as small as O(0.1) as long as F_L compensates a significant portion of the ageostrophic F_C and it satisfies $F_L \gg F_I$ and $F_L \gg F_V$. If $\Lambda \ll 1$ while the magnetic field could be self-sustained, it is called a weak field dynamo.

In the MoSST model, the magnetic field is nondimensionalized by $\sqrt{\Omega\mu\rho\eta}$, thus Equation 9 becomes $\Lambda=B^2$ in the nondimensional form. In our numerical results of $R_a=12,000$, B is averaged as 0.36 for all Ekmans, then we have $\Lambda\sim0.13$, which supports that they are weak field dynamos, but the possibility that a MAC balance exists cannot be ruled out according to Λ . The force balance according to Λ could be misleading (Soderlund et al., 2012) since that is only a rough order estimation. The real force balance should be based on each force's exact calculation in Equation 8 with the numerical results. By following Kuang (1999), we use the local force defined by (taking F_L as example)

$$F_{L\varphi}(r,\theta) = \int_{0}^{2\pi} F_{L}(r,\theta,\varphi) d\varphi = \int_{0}^{2\pi} \nabla \times \mathbf{B} \times \mathbf{B} d\varphi, \tag{10}$$

to study the exact force balance. The final Lorentz force F_L is the RMS value of $F_{L\varphi}$, and other forces are treated the same as F_L . Force balance (except F_P since that we are only interested in the ageostrophic part) results for different E are plotted in Figure 3.

As can be seen from Figure 3, all forces vary nonmonotonically with E except that F_A (green) is kept constant since the driving force (measured by R_a) doesn't change. The Coriolis force F_C (black) is always dominant by at least one order for all E, which indicates that they are all in the QG state. The Lorentz force F_L (red) is

DONG ET AL. 7 of 19

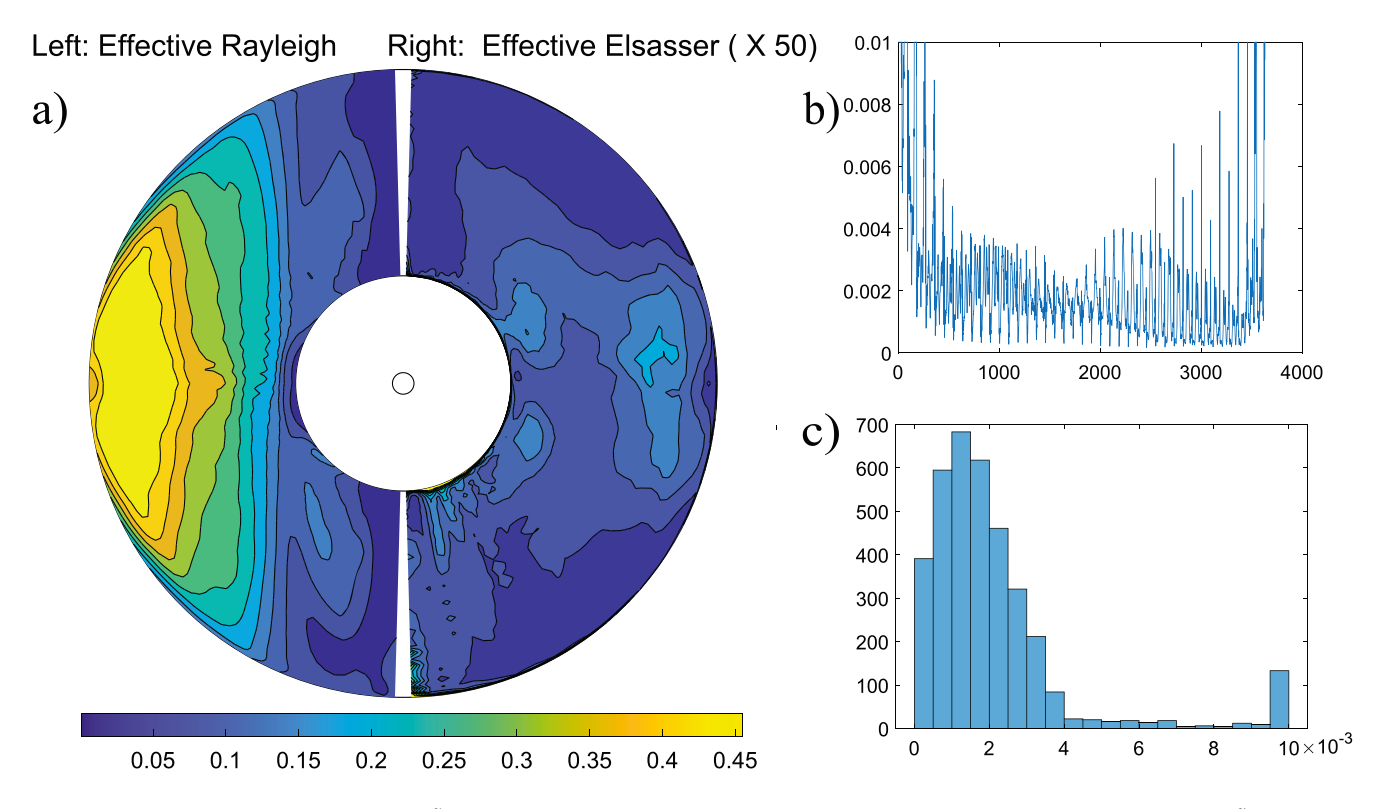


Figure 4. Snapshots of effective Elsasser number $\tilde{\Lambda}$ (the right part of Figure 4a, multiplied by a factor of 50) and effective Rayleigh number \tilde{R} (the left part of Figure 4a) for $R_a = 12,000$, $E = 2.5 \times 10^{-6}$. Figure 4b shows the distribution of $\tilde{\Lambda}$ with grid points at different r, θ , and Figure 4c shows the histogram distribution of $\tilde{\Lambda}$.

always about three orders smaller than the Coriolis force and at least one order smaller than other forces for all E, which proves that the systems are all far from MAC state. Furthermore, we divide the force balance into four regions: I, II, III, and IV. In region I, the ageostrophic F_C is mainly compensated by F_I (cyan) and F_A , which is called the QG-CIA balance (shorted for CIA). In region II, with the fast increase of F_I , the ageostrophic F_C is mainly compensated by F_I , which is called the QG-CI balance (shorted for CI). Similarly, we call region III the CIV and region IV the CV balance. Though fluctuating, F_V (blue) is generally increasing and becomes more and more significant in force balance with increasing of E, which is consistent with the increase of the fluid core's viscosity. When E decreases toward the real value for physical Earth, the system is expected to enter into a CIA balance in this weak field regime.

To check if there is a local distribution of the MAC state, we calculated the local effective Elsasser number $\tilde{\Lambda}$ and effective Rayleigh number \tilde{R} defined as (Kuang, 1999):

$$\tilde{\Lambda} = \frac{\int_0^{2\pi} \left| \nabla \times \left(\boldsymbol{J} \times \mathbf{B} \right) \right| d\varphi}{\int_0^{2\pi} \left| \hat{\sigma}_z \boldsymbol{u} \right| d\varphi + \int_0^{2\pi} \left| \nabla \times \left(\boldsymbol{J} \times \mathbf{B} \right) \right| d\varphi}, \tag{11}$$

$$\tilde{R} = \frac{\int_0^{2\pi} \left| R_a \nabla \Theta \times \mathbf{r} \right| d\varphi}{\int_0^{2\pi} \left| \hat{\sigma}_z \mathbf{u} \right| d\varphi + \int_0^{2\pi} \left| R_a \nabla \Theta \times \mathbf{r} \right| d\varphi}.$$
(12)

The curls in the above two equations are used to get the ageostrophic force. When $\tilde{\Lambda}=0.5$ means that the ageostrophic Lorentz force is comparative to the ageostrophic Coriolis force, and it is similar for \tilde{R} . Snapshot of $\tilde{\Lambda}$ and \tilde{R} distribution for $R_a=12,000$, $E=2.5\times 10^{-6}$ is shown in Figure 4. As can be seen from Figure 4a, $\tilde{\Lambda}$ (magnified by 50 times) is very small as a whole, though some relatively large values (>0.02) appear near the rotational axis. In contrast, \tilde{R} is generally large (>0.25), especially outside the tangent cylinder (TC,

DONG ET AL. 8 of 19

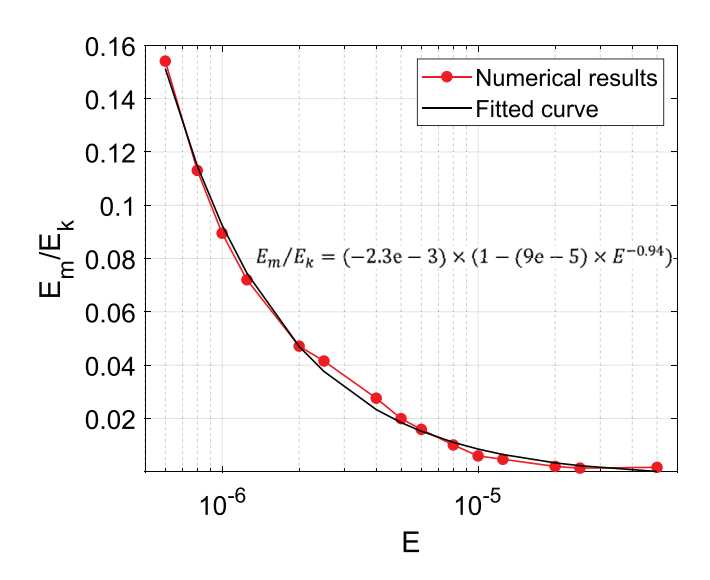


Figure 5. The ratio between magnetic energy density and kinematic energy density for $R_a = 12,000$. Red and black lines are for numerical and fitted results, respectively.

whose axis coincides with the rotation axis and tangents with the inner core at ICB). Both of $\tilde{\Lambda}$ and \tilde{R} show symmetry about the equator to a large extent. Figure 4b shows the distribution of $\tilde{\Lambda}$ with grid points of different r (from r_{io} to r_o), θ (from 0 to π / 2). There are some relatively obvious $\tilde{\Lambda}$ near the ICB. The histogram distribution of $\tilde{\Lambda}$ is plotted in Figure 4c, which shows that most areas have a typical $\tilde{\Lambda}$ of about 2×10^{-3} . Figure 4 indicates that the ageostrophic Coriolis force is mainly compensated by F_A outside TC but by F_I inside TC. F_L only plays a negligible role in the force balance in this weak field regime.

The ratio between magnetic energy density (E_m) and kinematic energy density (E_k) is another criterion to evaluate dynamo states. In a strong field dynamo, usually one has $E_m \gg E_k$ (at least two orders). The energy ratio is calculated by

$$\frac{E_m}{E_k} = \frac{B^2 / 2\mu}{\rho u^2 / 2} = R_o \frac{B^2}{u^2}.$$
 (13)

We use the numerical results of Table 2 to calculate it and use Equation 4 to fit its variation, then get Figure 5. As can be seen, the energy ratio almost decreases monotonically with E by a fitted exponent of -0.94, which results from increasing of u but not decreasing of B (see Figure 2). Anoth-

er noticed character is that the magnetic energy is always smaller than the kinematic energy, proving that the system is in a weak field regime and far from a MAC balance.

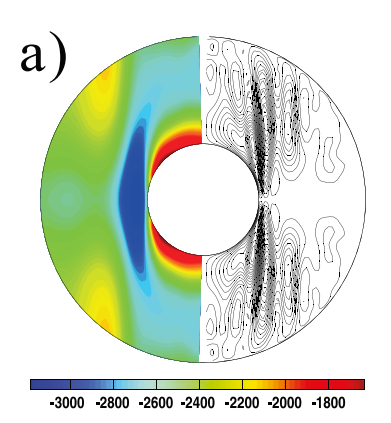
3.4. Field Configuration

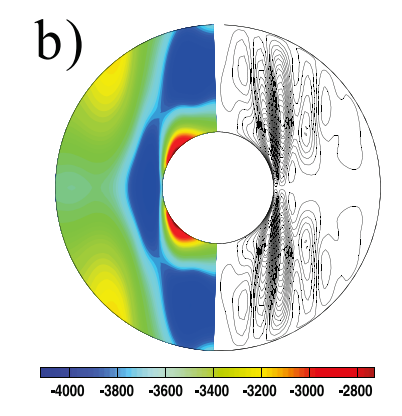
To figure out the effect of viscosity variation on the dynamo system, we mapped the flow fields with respect to different E, as shown in Figure 6. Each figure contains two halves. The left-colored half represents the axisymmetric (m = 0) toroidal flow, and the right half represents the axisymmetric poloidal flow. The results are all time-averaged outputs over one τ_f The toroidal flow (\mathbf{u}_T) and poloidal flow (\mathbf{u}_P) are defined as

$$\mathbf{u} = \mathbf{u}_T + \mathbf{u}_P = \nabla \times T_u \mathbf{1}_r + \nabla \times \nabla \times P_u \mathbf{1}_r. \tag{14}$$

The left part of Figure 6 is the axisymmetric zonal component of velocity \mathbf{u}_{φ} , the right part is the axisymmetric streamline (Ψ_u) , defined by

$$\mathbf{u}_{S} = \mathbf{u}_{\varphi}(r,\theta) + \nabla \times \frac{\Psi_{u}}{c} \mathbf{1}_{\varphi}, \tag{15}$$





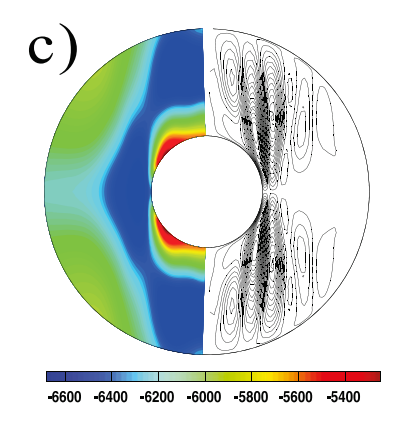


Figure 6. Variation in the axisymmetric velocity against different values of Ekman number in the meridian plane sections when $R_a = 12,000$. Figures 6a–6c, in correspond to the output at different values of Ekman number: $E = 2.5 \times 10^{-6}, 5 \times 10^{-6}, \text{and } 1.25 \times 10^{-5}, \text{ respectively}$. The left-colored half represents the axisymmetric (m = 0) toroidal flow, and the right linear half represents the axisymmetric poloidal flow.

DONG ET AL. 9 of 19

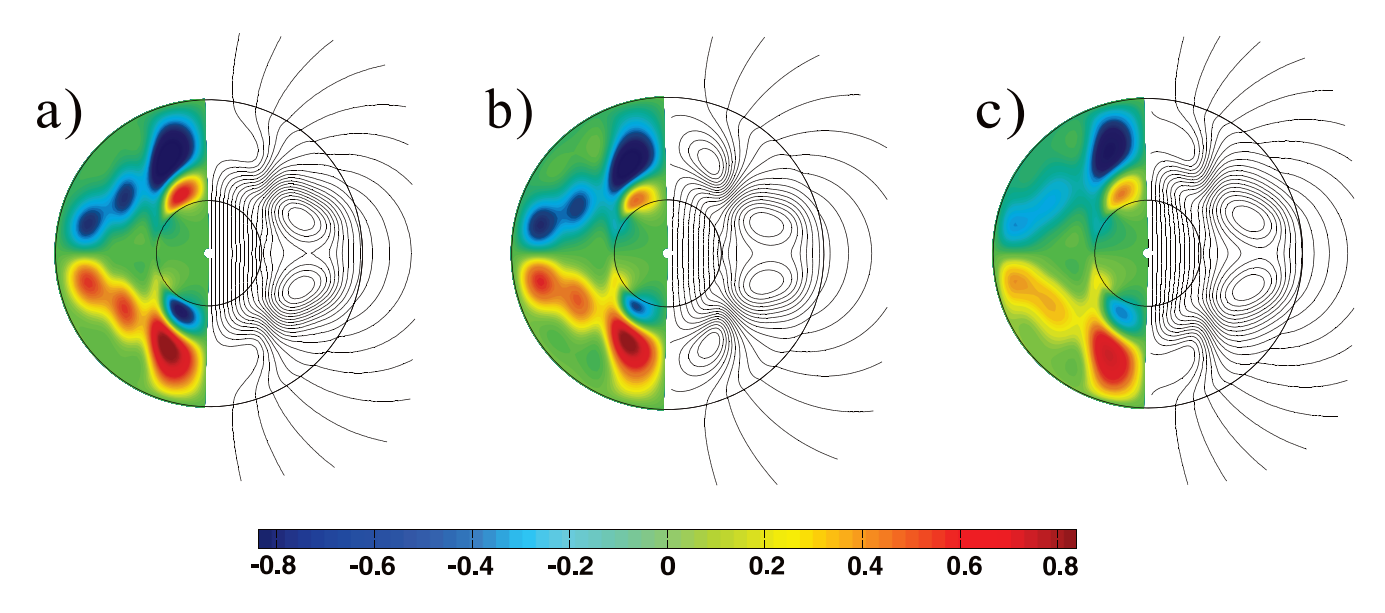


Figure 7. Variations in the axisymmetric magnetic field with different Ekman numbers when $R_a = 12,000$. Figures 7a–7c, corresponding to outputs with different Ekman numbers: $E = 2.5 \times 10^{-6}$, 5×10^{-6} , and 1.25×10^{-5} respectively. The left-colored half respects the axisymmetric (m = 0) toroidal field, and the right linear half represents the axisymmetric poloidal field.

where \mathbf{u}_S is the axisymmetric velocity, $s = r \cdot \sin \theta$ is the distance from the field point to Earth's rotation axis.

As can be seen from Figure 6, the mean flow velocity increases with E. When $E = 2.5 \times 10^{-6}$, the liquid iron flow mainly concentrates on the TC's profile. As E increases gradually, the flow concentrates on the TC and extends toward CMB on the equator plane. These two features are both reflected in the toroidal flow (left half). For the poloidal flow (right half), a significant increase of flow scales can be found both inside and outside the TC.

The axisymmetric magnetic field is shown in Figure 7. As can be seen, for the toroidal field, it could be locally strong, especially inside the TC, though the system is in a weak field regime as a whole. The toroidal field strength decreases and tends to concentrate in the TC with increasing of E. There appears no significant difference for the poloidal magnetic field, and the dipolar field outside CMB (where only a poloidal field exists) all dominate.

3.5. Numerical Results of a Quasi-MAC Regime

Our $R_a = 12,000$ results are all proven to be in the weak field regime. To study the strong field mode, we gradually increase R_a and two typical values, $R_a = 30,000$ and 50,000 are selected and listed in Table 3. Dynamo simulations at higher R_a^S consumed more computational cost to evolve, thus fully developed results

Table 3 Output Results With Different Values of Ekman Number Under the Strong Field							
	Ekman	и	В	Θ	l_u	l_B	l_{Θ}
$R_{\rm a} = 30,000$	5.00e-06	362	1.4464	0.0907	0.0811	0.0640	0.3800
	6.00e-06	337	1.4593	0.0907	0.0790	0.0625	0.3791
	8.00e-06	381	1.4918	0.0909	0.0934	0.0660	0.3765
	1.25e-05	382	1.4088	0.0910	0.0997	0.0661	0.3750
$R_{\rm a} = 50,000$	2.50e-05	364	1.9885	0.0922	0.0952	0.0657	0.3619
	5.00e-05	390	1.8377	0.0923	0.1127	0.0681	0.3612
	1.25e-04	424	1.2897	0.0924	0.1353	0.0613	0.3617

DONG ET AL. 10 of 19

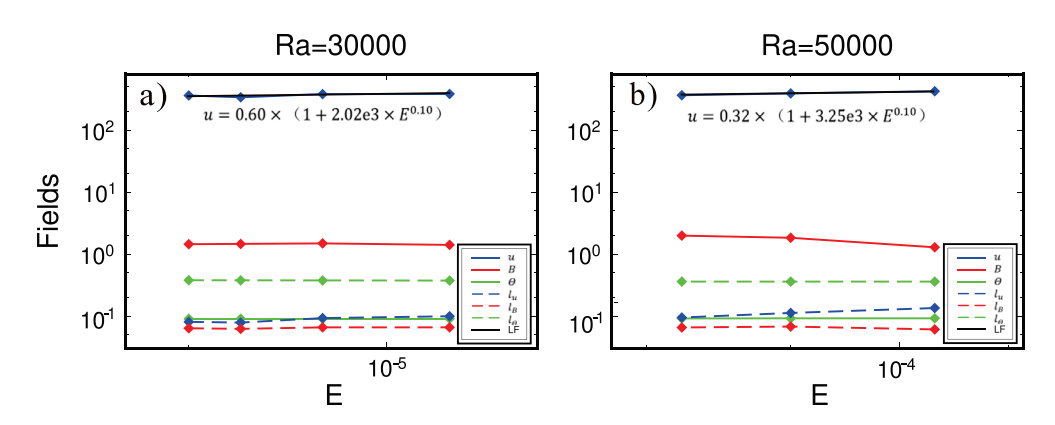


Figure 8. Variations of fields and their typical scales with E for $R_a = 30,000$ and $R_a = 50,000$. Different lines and colors represent different fields and forces, as shown in the legend.

are not many here. Compared to results of $R_a=12,000$ in Table 1, when R_a increases, significant variations appear in both of B and u: B increases by about five times but u decreases by over an order, which manifests energy transfer and conservation (not rigorous since there are also variations in input and dissipated energy). As for variations with E, u, and l_u appear monotonically increase while B appears monotonically decrease for $R_a=50,000$, but all of them vary nonmonotonically for $R_a=30,000$. Θ increases slightly and monotonically, and l_B , l_{Θ} fluctuate with E for both of two R_a^S .

Figure 8 shows variations of the fields and their typical length scales with E. The exponential relationship between u and the E (viscosity) is

$$u = 0.60 \times (1 + 2.02 \text{e}^{3 \times E^{0.10}}) (R_a = 30,000),$$
 (16)

$$u = 0.32 \times (1 + 3.25 \text{e}3 \times E^{0.10}) (R_a = 50,000).$$
 (17)

The exponential factor is about 0.10 for both equations, which is much smaller than that for the weak field regime (0.52). This suggests that the influence of viscosity on the velocity field is much little under a stronger field. The impact of E on B when $R_a = 30,000$ is as small as that in the weak field regime. While

 $R_a = 50,000$, B is significantly weakened with E, the association factor is -0.20. The relationship between l_u and E for $R_a = 30,000$ and $R_a = 50,000$ are, respectively

$$l_u = (6.16e - 4) \times (1 + 1.00e4 \times E^{0.36}) (R_a = 30,000),$$
 (18)

$$l_u = (9.36e - 4) \times (1 + 1.00e4 \times E^{0.22}) (R_a = 50,000).$$
 (19)

Next, we check the force balance, taking $R_a=50,000$ for example. First, the Elsasser numbers ($\Lambda=B^2$) are O(1) (from 1.6 to 4), which indicates that the system may be in a strong field regime. Second, we calculated the RMS values of the local forces defined by Equation 10 and normalized all of them by F_C . The results are shown in Figure 9. As can be seen, rvc increases monotonically with E and the other three force ratio fluctuate. With increasing of E, rvc varies from $\sim 15\%$ to 50%. rmc and rvc are always comparable to each other, and they are about 20%. ric is as small as 5%, which indicates that inertial plays a tiny role in the force balance. According to the above variances of force ratios, Figure 9 is divided into three regions: I-MAC, where the ageostrophic F_C is mainly compensat-

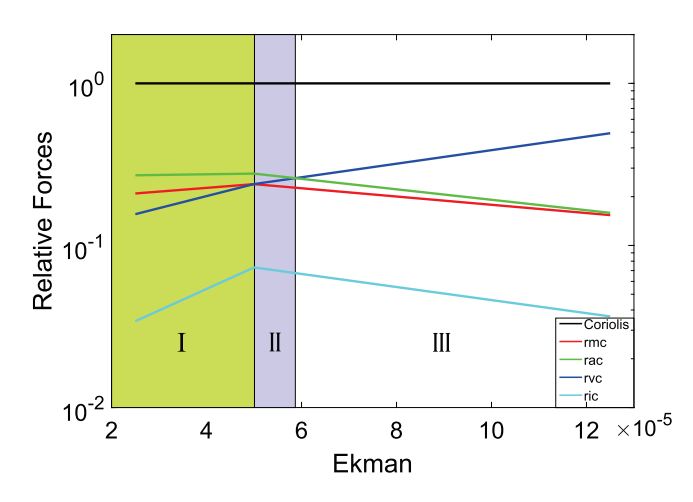


Figure 9. Relative forces for different E when $R_a = 50,000$. Different colors represent different forces, as shown in the legend, of which the forces are normalized by F_C , rmc = F_L / F_C , rac = F_A / F_C , rvc = F_V / F_C , and ric = F_L / F_C .

DONG ET AL. 11 of 19



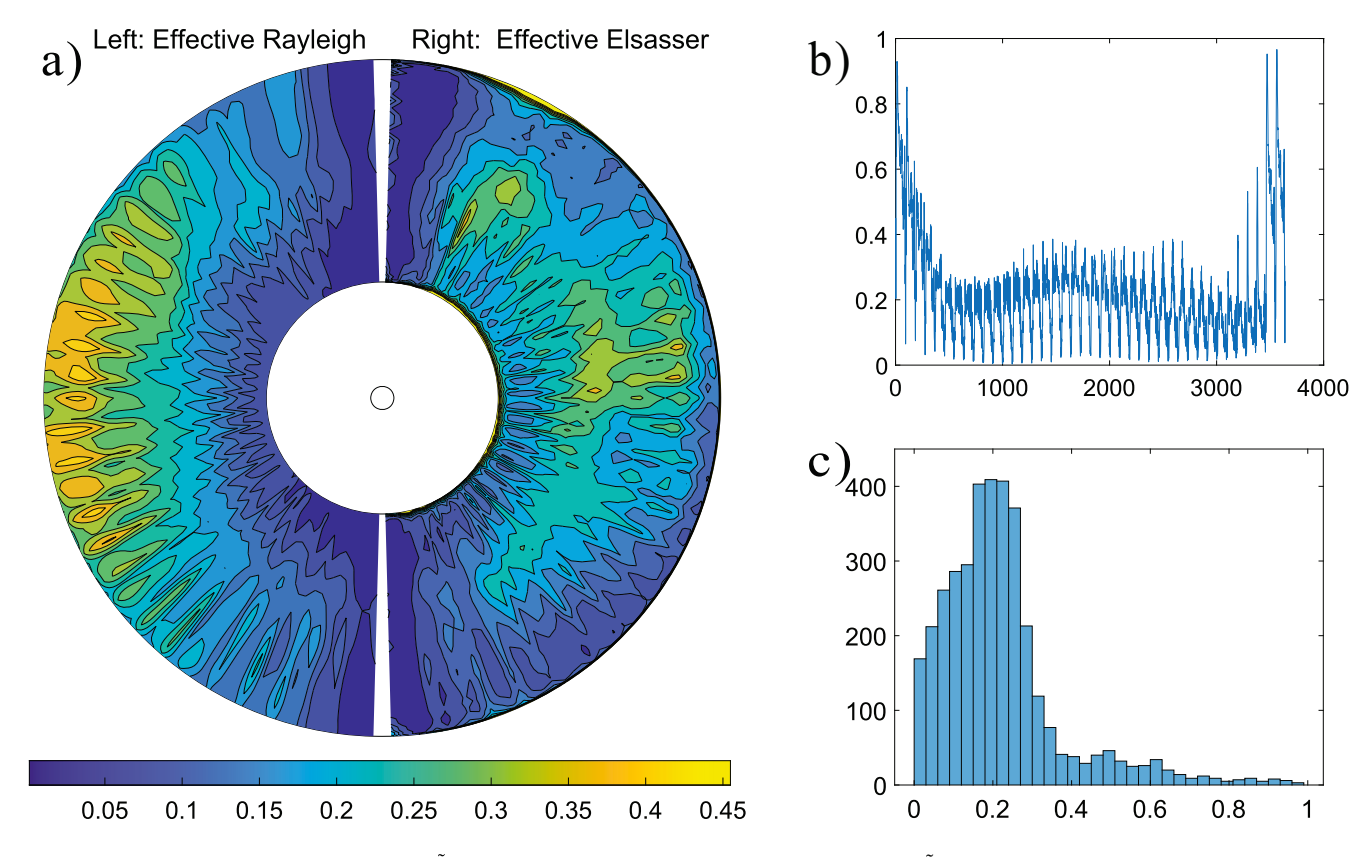


Figure 10. Snapshots of effective Elsasser number $\tilde{\Lambda}$ (right in Figure 10a) and effective Rayleigh number \tilde{R} (left in Figure 10a) for $R_a = 50,000$ and $E = 2.5 \times 10^{-5}$. Figure 10b shows the distribution of $\tilde{\Lambda}$ with grid points at different r, θ , and Figure 10c shows the histogram distribution of $\tilde{\Lambda}$.

ed by $F_A + F_L$; II-MAVC, where the ageostrophic F_C is mainly compensated by $F_A + F_L + F_V$ and III-VC, where the ageostrophic F_C is mainly compensated by F_V . As E decreases toward the real value, the system is expected to be more close to a MAC state, which is consistent with geodynamo theoretical consensus.

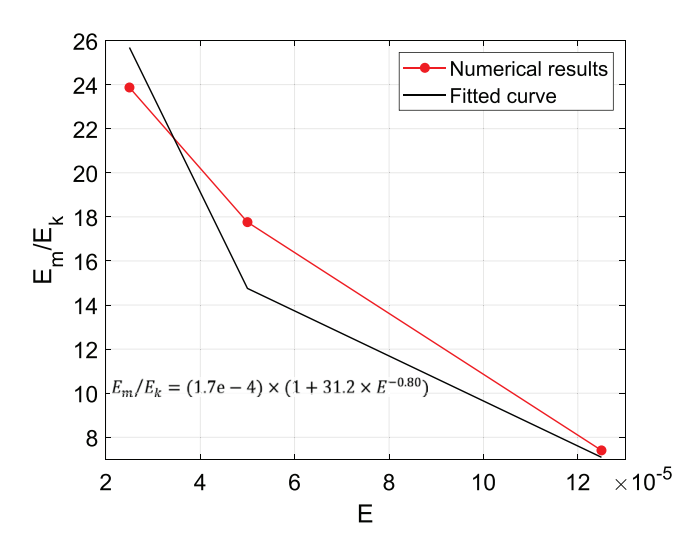


Figure 11. The ratio between magnetic energy density and kinematic energy density for $R_u = 50,000$. Red and black lines are for numerical and fitted results, respectively.

We call the two solutions for $R_a = 50,000$ ($E = 2.5 \times 10^{-5}$ and 5×10^{-5}) in a quasi-MAC state, since F_V still plays a role but will turn into more and more insignificant with decreasing of E.

Third, the local quasi-MAC balance is checked by the effective Elsasser number $\tilde{\Lambda}$ and effective Rayleigh number \tilde{R} defined in Equations 11 and 12. Results are shown in Figure 10. As can be seen, the ageostrophic F_C is mainly compensated by F_L near ICB, by F_A near CMB, and by F_V near the rotational axis (refer to Figure 9). Figure 10b shows that large $\tilde{\Lambda}$ distributes at ICB and some part of CMB, while Figure 10c shows that $\tilde{\Lambda}$ has a typical value of \sim 0.2.

Lastly, we check the energy density ration E_m / E_k , as defined by Equation 13, using the RMS u and B listed in Table 3. The result is shown in Figure 11. As can be seen, when E increases from 2.5×10^{-5} to 1.25×10^{-4} , the energy ratio decreases from 23.9 to 7.4. As E varies, the magnetic energy is larger than the kinematic energy by about an order. This again proves that the system is in a quasi-MAC balance. If E decreases to the real value, this ratio is expected to become even larger, consistent with MAC's theoretical predictions or strong field dynamo regime (Schaeffer et al., 2017).

DONG ET AL. 12 of 19



4. Discussions

The outer core flow increases with viscosity, especially under a weak field, significantly different from the hydrodynamics system's general concept. Previous studies on geodynamo proposed the same conclusion. Here, we discuss the similarities and differences with previous studies and analyze the variation mechanism.

4.1. Influence of Viscosity on the Critical Driving Force and Flow Scales

The fluid motion in the outer core is strongly affected by Earth's rotation, and the rotation, therefore, induces a fundamental change in the dynamo pattern of the outer core. The leading-order momentum equation is the geostrophic equilibrium (which can also be seen in Figure 3, where Coriolis forces dominate throughout), where only Coriolis forces and the pressure gradient are retained for Equation 8

$$\mathbf{1}_{z} \times \mathbf{u} = -\nabla P. \tag{20}$$

Taking the curl of both sides of Equation 20, we have

$$\frac{\partial \mathbf{u}}{\partial z} = 0. \tag{21}$$

This shows that dynamo flow is essentially two-dimensional and is constant along the rotation axis, namely the Taylor-Proudman (T-P) theorem. Taylor (1963) first proposed that the convection pattern is a series of parallel cylindrical convection rolls parallel to the rotation axis and rotating along the rotation axis. However, in a closed spherical system, this form of flow can neither transfer heat to the outside nor maintain the dynamo process. Therefore, the T-P constraint must be broken so that the governing equation's first-order term is ageostrophic. To study the influence of viscosity alone, by neglecting F_A , F_L and F_I (e.g., Region IV in Figure 3 and Region III in Figure 9), taking the curl of Equation 8 and obtaining the vorticity equation, and taking the radial component of the vorticity equation, then we obtain

$$\frac{\partial u_r}{\partial z} = E \mathbf{1}_r \cdot \nabla^2 \boldsymbol{\omega},\tag{22}$$

where $\omega = \nabla \times u$ is vorticity. From Equation 22, it is apparent that, under the $u_r = 0$ boundary conditions, larger E will result in larger u_r . This may partly and qualitatively explain why u increase with E or v. u is also affected by other velocity components, together with the vorticity in the right-hand side of the equation and other forces. Therefore, u does not exhibit a simple proportional relationship with E.

From another point of view, increasing the viscosity help break the T-P constraint by lowering the critical Rayleigh number R_{a_c} , Which marks the critical driving force for thermal convection in a fast-rotating system. Chandrasekhar (1981) introduced the steady state rotational thermal convection theory and presented that

$$R_{a_c} = 3E^{-\frac{4}{3}} \left(\frac{\pi^2}{2}\right)^{2/3}.$$
 (23)

Since the definition of R_a is different from MoSST, so Equation 23 can be derived as $R_{a_c} \sim v^{-1/3}$ or $R_{a_c} \sim E^{-1/3}$. Roberts and Chandrasekhar (1968) then deduced that $R_{a_c} = O\left(E^{-1/3}\right)$. Later on, with their numerical simulations of R_{a_c} and E, Kuang and Bloxham (1999) proposed that $R_{a_c} \approx 10.1E^{-1/3}$, and Roberts and King (2013) proposed that $R_{a_c} \approx 8.696E^{-1/3}$. All these results indicate that convection occurs more easily with increasing viscosity. Meanwhile, core convections also become more active with larger E.

Some studies have also analyzed the convective roll diameter l_{conv} , and found that $l_{\text{conv}} \sim E^{1/3}$ H, where H = $r_o - r_i$ is the spherical shell thickness (Aurnou et al., 2015; Chandrasekhar, 1981; Johnson & Constable, 1998; Roberts & King, 2013). Figure 12 shows the sketch map of convection roll diameter l_{conv} and the

DONG ET AL. 13 of 19

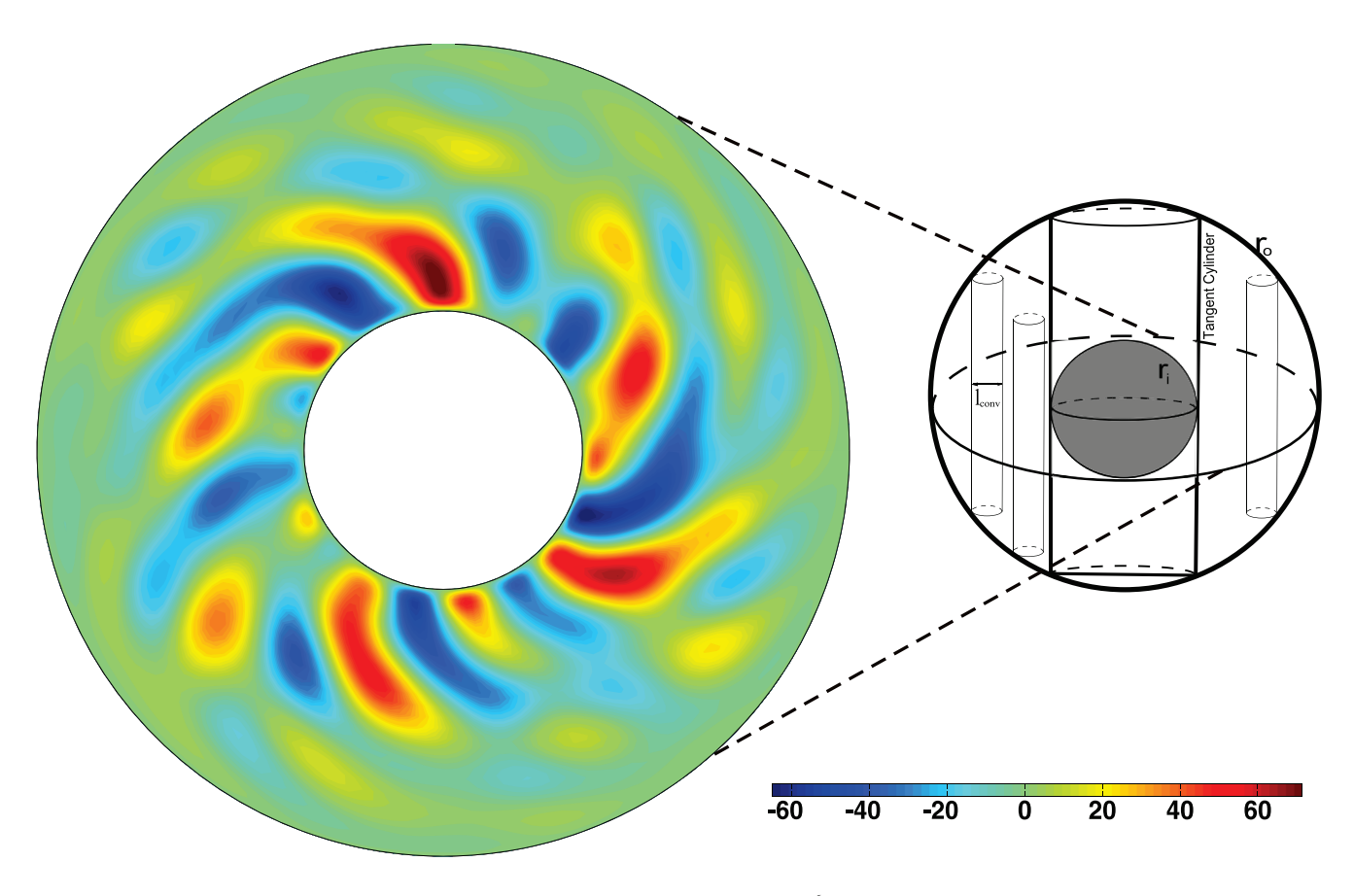


Figure 12. Distribution of radial velocity u_r on the equatorial plane ($R_a = 12,000, E = 2.5 \times 10^{-6}$). The red and blue stand in different velocity directions. The convection columns are paralleled to the TC, which is shown on the right. TC, tangent cylinder.

previously mentioned TC in the right. Using our results of $R_a = 12,000$ (referred to Figure 2), the increase of viscosity facilitates the flow velocity and stretches fluid flow in the outer core.

Although researches on E through R_{a_c} and $l_{\rm conv}$ are many, only King and Buffett (2013) provided a quantitative result on the effect of E on u by $u \sim C^{1/2}E^{1/3}$. However, this result cannot be simply interpreted as the direct relationship between velocity and viscosity in the outer core because their work is based on $R_e \sim C^{1/2}E^{1/3}$, where $R_e = ul / v$ is the Reynolds number and $C = PH^3 / A\rho_0 v^3$ is the convection energy. If we assume that P and A are independent of v, we can derive: $u \sim v^{-1/6}$. This inference contradicts to the dynamo system. Therefore, the most significant contribution of this study is that it provides the only direct and reliable quantitative relationship between u and v to date by fitting numerical dynamo data.

The variation of with ν is weaker than other studies, especially under a weak field (exponential factor = 0.12). The convective column results from the ideal approximation, and realistic dynamo convection is complex and affected by various forces. It can also be seen from the distribution of u_r on the equatorial plane, as shown in Figure 12, where convection rolls are elongated and twisted in the radial direction. They are no longer an ideal cylindrical shape, and their spatial scale could not be simply represented by the diameter of convection rolls anymore.

When the T-P constraint is broken, the convection becomes quasi-three-dimensional. There is a radial component, whose amplitude is only 2% of u_{φ} (referred to Figure 6). Stress-free boundaries lead to larger zonal flows, so it might also explain why our results differ from others researches in that most studies use the no-slip boundaries conditions, which will be affected by the Ekman layer (Wicht & Sanchez, 2019; Yadav et al., 2016). However, this 2% radial portion is critical to the generation and maintenance of the geodynamo process. Were it not for this small u_r , the heat cannot be transported outside, and the flow will degenerate

DONG ET AL. 14 of 19



into two-dimensional. According to Cowling's (1933) antidynamo principle, two-dimensional flow cannot maintain the dynamo process.

4.2. The Role of Viscosity on the Magnetic Field and Flow Field

Next, we focus on the determining factors for the magnitude of the magnetic field. As is mentioned, geodynamo is speculated to operate at a strong field regime, such that B satisfies $\Lambda \sim O(1)$. In this situation, the force balance determines the magnitude of B. Starchenko and Jones (2002) proposed that it is rather the driving force and force balance than diffusion coefficients that determine the flow velocity and the magnetic field. Christensen and Aubert (2006) assumed that the diffusion effects do not play a major role in the governing equations, and they found that the available energy (represented by the flow Rayleigh number R_{a_Q}), rather than the force balance, determined the magnitude of the magnetic field. Christensen (2010) summarized scaling laws for the magnetic field and proposed that the magnitude of B depended on the available energy flux, which could overcome the ohmic loss. They argued that rotation only determines whether a dipole field is generated. Jones (2011) also used the R_{a_Q} concept to provide an estimation of the velocity field and the magnetic field.

In this study, under the weak field regime ($R_a=12,000$), the magnetic field B only changes by 22.3% when E varies by two orders of $\left(6\times10^{-7}\le E\le 5\times10^{-5}\right)$, which partly supports the conclusion that the magnitude of B is not strongly associated with viscosity. While when, the magnetic field is annihilated, indicating that ν has a significant impact on magnetic field generation upon a critical point (via R_a^c to R_a^m). $E<6\times10^{-7}$ For quasi-MAC regime, the magnetic field decreases significantly with (decreases by 35.4% as E is 5 times larger), and the increase of flow is also noticeable (16.5%), indicating that the influence of viscosity on the flow and magnetic field cannot be ignored.

4.3. The Role of Viscosity on Geodynamo Force Balance

Geodynamo is expected to run in the MAC state. The existing geodynamo simulations can explain a couple of observations in principle. Those model parameters adopted in simulations are still far from physical. It leads to active arguments on whether existing geodynamo models can run in a good regime representing the physical Earth. After checking the exact force balance or fitting the numerical data, studies showed that viscosity, instead of the magnetic field, plays a major role in the force balance for most of the existing geodynamo simulation results (King & Buffett, 2013; Oruba & Dormy, 2014; Soderlund et al., 2012). Most existing dynamo models are, in fact running in VAC, not MAC balance (Yadav et al., 2016), and a real MAC state is hard to reach except using a more physical parameter (e.g., $R_a = 5,000R_a^c$, $E = 10^{-7}$) and simulating at very high resolution (Aubert, 2019; Schaeffer et al., 2017).

Variations of ν can bring substantial changes to the force balance. In the weak field regime, as is shown in Figure 3, as E increases, the system gradually transfers from CIA mode to VC mode. CIA mode may result in a strongly driven but nonmagnetic system or multiple dynamo regimes (Soderlund et al., 2012). When $E > 3 \times 10^{-6}$, F_V grows more and more obvious in the force balance. Though fluctuates with E, F_L is always fairly weak (Figure 3), rendering it only plays a minor role in the force balance, and the dynamo state is far from a MAC balance (Figure 4). The energy ratio between E_m and E_k increases as E decreases, while we always have $E_m < E_k$ in our parameter space (Figure 5). In the quasi-MAC regime, as E increases, the system transfers from a quasi-MAC mode to VC mode (Figure 9). When $E > 5 \times 10^{-5}$, F_C grows more and more important in the force balance. When $E < 5 \times 10^{-5}$, the system enters into a quasi-MAC regime, verified by the force ratio distribution (Figure 9), the local effective \tilde{R} and $\tilde{\Lambda}$ distribution (Figure 10), and the energy ratio (Figure 11). As E decreases toward the real value, F_L plays a more and more important role in core dynamics, and the system is expected to evolve into a real MAC regime, as is estimated theoretically.

The exponent of scaling relation of u and v decreases from 0.52 for $R_a = 12,000$ (Figure 2) to 0.10 for $R_a = 50,000$ (Figure 8), which indicates that the effects of viscosity on fluid velocity is much smaller for strong-driven and in the quasi-MAC regime than the weakly driven and in the weak field regime. The

DONG ET AL. 15 of 19



reason is not that the relative important of F_V is smaller in a quasi-MAC balance (compare Figure 3 with Figure 9), but that F_L enters into the first-order ageostophic balance (Figure 10) and replaces F_I , and much of the kinematic energy is transferred into the magnetic energy (compare Figure 5 with Figure 11).

4.4. The Effect of the Hyperdiffusion Assumption

Hyperdiffusion could be avoided, while the temporal and spatial resolution must be improved. To improve the computational efficiency, especially simulate at high R_a and low E, hyperdiffusion is retained in this study. Hyperdiffusion mainly suppresses the development of small-scale convection and has no significant effect on large-scale flow, which is one of the major reasons that the typical spatial scale of various physical fields is all large in our simulations. Researches on the influences of hyperdiffusion are many. For example, Zhang and Jones (1997) found that hyperviscosity significantly increased the equivalent Ekman number and changed the convection kinetics. Grote et al. (2000) concluded that hyperdiffusion could affect the magnetic field generation mechanism and even reverse polarity.

In our simulations, we choose $l_0=4$, $\epsilon=0.05$ in Equation 3. To give a proper quantification of the hyper-diffusion and implication to the scaling laws and get a clear understanding of the hyperdiffusion effects on the MoSST model, a general assessment is made in this work.

To obtain quantitative properties and provide quantified "large-scale patterns" which will be used to derive the scaling laws, we should find the highest spherical harmonic degree L^H , above which the hyperdiffusive effect will be dominant. Only use the part of the solutions with spherical harmonic coefficients of degrees $l \le L^H$ in our analysis. With this approach, we would hope to find asymptotic behaviors of the "large-scale" dynamo solutions. Then we can see the effective Ekman number E^H to account for the hyperdiffusivity used in the simulation, and derive the scaling laws with respect to E^H .

The relative importance of the hyperdiffusivity for large-scale solutions ($l \le L^H$) can be described by the ratios of the following viscous dissipation terms,

$$E_{P}^{v} = -E \int dr \sum_{0 \le m \le l}^{L^{H}} \frac{l^{2} (l+1)^{2}}{r^{4}} \left\{ \left| \frac{\partial v_{l}^{m}}{\partial r} \right|^{2} + \frac{l(l+1)}{r^{2}} \left| v_{l}^{m} \right|^{2} \right\}, \tag{24}$$

$$E_T^{\nu} = -E \int dr \sum_{0 \le m \le l}^{L^H} \frac{l^2 (l+1)^2}{r^4} \left\{ \left| \frac{\partial \omega_l^m}{\partial r} \right|^2 + \frac{l(l+1)}{r^2} \left| \omega_l^m \right|^2 \right\}, \tag{25}$$

$$E_{P}^{vH} = -E \int dr \sum_{0 \le m \le l}^{L^{H}} \alpha(l) \frac{l^{2}(l+1)^{2}}{r^{4}} \left\{ \left| \frac{\partial v_{l}^{m}}{\partial r} \right|^{2} + \frac{l(l+1)}{r^{2}} \left| v_{l}^{m} \right|^{2} \right\}, \tag{26}$$

$$E_T^{\nu H} = -E \int dr \sum_{0 \le m \le l}^{L^H} \alpha(l) \frac{l^2 (l+1)^2}{r^4} \left\{ \left| \frac{\partial \omega_l^m}{\partial r} \right|^2 + \frac{l(l+1)}{r^2} \left| \omega_l^m \right|^2 \right\}, \tag{27}$$

where v_l^m and ω_l^m are the poloidal and toroidal spherical harmonic coefficients of degrees l and orders m, respectively.

DONG ET AL. 16 of 19



Table 4The Values of the L^H and Effective Ekman Number E^H

R_a	E	E^{H}	L^H
$R_a = 12,000$	6.00E-07	1.82E-5	6
	8.00E-07	1.99E-5	6
	1.00E-06	2.06E-5	6
	1.25E-06	2.22E-5	6
	2.00E-06	2.79E-5	5
	2.50E-06	4.12E-5	6
	4.00E-06	5.79E-5	6
	5.00E-06	8.46E-5	7
	6.00E-06	1.13E-4	6
	8.00E-06	1.41E-4	6
	1.00E-05	2.81E-4	6
	1.25E-05	4.75E-4	5
	2.00E-05	8.08E-4	6
	2.50E-05	1.00E-3	6
	5.00E-05	2.14E-3	7
$R_a = 30,000$	5.00E-06	2.14E-4	5
	6.00E-06	2.58E-4	6
	8.00E-06	3.44E-4	6
	1.25E-05	5.36E-4	6
$R_{\rm a} = 50,000$	2.50E-05	1.08E-3	6
	5.00E-05	2.15E-3	6
	1.25E-04	5.38E-3	6

The maximum degree L^H can then be determined if the ratios $\beta = \left|\left(E_P^{vH} + E_T^{vH}\right)/\left(E_P^v + E_T^v\right)\right| \le 0.1$, to make sure the hyperdiffusion is of secondary importance. The effective Ekman number E^H can also be calculated based on Equations 24–27:

$$E^{H} = E \frac{E_{P}^{\nu H} + E_{T}^{\nu H} + E_{P}^{\nu} + E_{T}^{\nu}}{E_{P}^{\nu} + E_{T}^{\nu}}.$$
 (28)

The L^H and E^H are calculated and listed in Table 4. As can be seen, in the weak field regime, the effective Ekman numbers are overall 10-30 times the Ekman numbers used in the analyses as mentioned earlier. Though this will affect the quantitative results for each E, it would not change the whole regularity (e.g., the exponential in the scaling law). The effects of hyperdiffusion are equivalent to multiply each E in our scaling laws by a factor of ~ 20 . The maximum degree for hyperdiffusion L^H is about 5–7, and scales smaller than these ($l > L^H$) will be affected substantially. These effects should be kept in mind for references to this study.

5. Conclusions

To systematically study the effects of viscosity on the geomagnetic field dynamo both in a weak and strong field, we adopt the newly developed MoSST model to perform numerical experiments on the dynamo process. The advantage of the MoSST model is that, since the magnetic diffusion time is used as the typical time scale, ν is only included in E, making the variation of E equivalent to that of ν . Major conclusions reached through our numerical investigations are as follows

- 1. The role of core viscosity on dynamo is non-negligible and different for weak field and quasi-MAC regime. In a weak field regime, variations of ν may affect the fluid velocity and its typical length scale (Figure 2), the force balance (Figure 3), energy ratio (Figure 5), configurations of flow (Figure 6), and magnetic field (Figure 7). The magnitude of B is not so sensitive to ν . While in the quasi-MAC regime, the effect of ν on u and l_u is much smaller, but B decreases fast with ν (Figure 8). The force balance varies solely with the relative importance of F_{ν} (Figure 9).
- 2. As ν decreases toward the real value, the dynamo system involves into CIA balance for the weak field regime and MAC balance for the quasi-MAC regime. Our scaling relations are different from existing scaling laws not only in the scaling form but also in the exponent. For example, in a CIA state, former studies (King & Buffett, 2013) gave $u \sim E^{0.2}$, while we got $u = 0.11 \times \left(1 + 1.43 \text{e}7 \times E^{0.52}\right)$ for the weak field regime. By contrast, in a MAC state, former studies gave $u \sim E^{0.5}$ while we got $u = 0.32 \times \left(1 + 3.25 \text{e}3 \times E^{0.10}\right)$ in the quasi-MAC regime.
- 3. The drop of fitted exponent from 0.52 for the weak field to 0.10 for the quasi-MAC state is not attributed to the relative importance of F_V becomes weaker (comparing Figures 3 and 9), but because that F_L instead of F_I plays a more important role in the latter regime.

There are limitations in this study. When changing the value of E and R_a . The other two-dimensionless parameters (R_o and q_κ) are kept constant. Changes in them may quantitatively affect the conclusions drawn here. Solutions of the quasi-MAC state maybe not sufficient, and the resolutions need to be improved. Hyperdiffusion still has effects on core dynamics especially for smaller length scales (l > 7). We will aim to solve these in future research.

DONG ET AL. 17 of 19



Data Availability Statement

The relevant data are in Tables 2-4, and the simulation data can be download at https://zenodo.org/record/4561773.

Acknowledgments

This research is supported by National Natural Science Foundation of China (41725017, 42004049, and 42074072), the National Basic Research Program of China under Grant No. 2014CB845906, the Special Fund of the Institute of Geophysics, China Earthquake Administration (Grant Nos. DQJB19B01 and DQJB19B12). The authors would like to thank the Editor Michael Bostock, the Associate Editor, Prof. Weijia Kuang, and another anonymous reviewer for their constructive comments which have greatly improved the quality of this study.

References

- Aubert, J. (2018). Geomagnetic acceleration and rapid hydromagnetic wave dynamics in advanced numerical simulations of the geodynamo. Geophysical Journal International, 214(1), 531–547. https://doi.org/10.1093/gji/ggy161
- Aubert, J. (2019). Approaching Earth's core conditions in high-resolution geodynamo simulations. *Geophysical Journal International*, 219(Suppl 1), S137–S151. https://doi.org/10.1093/gji/ggz232
- Aubert, J. (2020). Recent geomagnetic variations and the force balance in Earth's core. *Geophysical Journal International*, 221(1), 378–393. https://doi.org/10.1093/gij/ggaa007
- Aubert, J., Gastine, T., & Fournier, A. (2017). Spherical convective dynamos in the rapidly rotating asymptotic regime. *Journal of Fluid Mechanics*, 813, 558–593. https://doi.org/10.1017/jfm.2016.789
- Aurnou, J. M., Calkins, M. A., Cheng, J. S., Julien, K., King, E. M., Nieves, D., et al. (2015). Rotating convective turbulence in Earth and planetary cores, *Physics of the Earth and Planetary Interiors*, 246, 52–71. https://doi.org/10.1016/j.pepi.2015.07.001
- Buffett, B. A. (2000). Earth's core and the geodynamo. Science, 288(5473), 2007-2012. https://doi.org/10.1126/science.288.5473.2007
- Calkins, M. A., Julien, K., & Tobias, S. M. (2017). Inertia-less convectively-driven dynamo models in the limit of low Rossby number and large Prandtl number. *Physics of the Earth and Planetary Interiors*, 266, 54–59. https://doi.org/10.1016/j.pepi.2017.03.003
- Calkins, M. A., Julien, K., Tobias, S. M., & Aurnou, J. M. (2015). A multiscale dynamo model driven by quasi-geostrophic convection. Journal of Fluid Mechanics, 780, 143–166. https://doi.org/10.1017/jfm.2015.464
- Chandrasekhar, S. (1981). Hydrodynamic and hydromagnetic stability. New York, NY: Dover Publications.
- Cheng, J. S., & Aurnou, J. M. (2016). Tests of diffusion-free scaling behaviors in numerical dynamo datasets. Earth and Planetary Science Letters, 436, 121–129. https://doi.org/10.1016/j.epsl.2015.12.004
- Christensen, U., Olson, P., & Glatzmaier, G. A. (1999). Numerical modeling of the geodynamo: A systematic parameter study. *Geophysical Journal International*, 138, 393–409. https://doi.org/10.1046/j.1365-246X.1999.00886.x
- Christensen, U. R. (2010). Dynamo scaling laws and applications to the planets. Space Science Reviews, 152(1-4), 565-590. https://doi.org/10.1007/s11214-009-9553-2
- Christensen, U. R., & Aubert, J. (2006). Scaling properties of convection-driven dynamos in rotating spherical shells and application to planetary magnetic fields. *Geophysical Journal International*, 166(1), 97–114. https://doi.org/10.1111/j.1365-246X.2006.03009.x
- Christensen, U. R., & Wicht, J. (2007). Numerical dynamo simulations. In *Treatise on geophysics* (pp. 245–282). Amsterdam: Elsevier. https://doi.org/10.1016/B978-044452748-6.00134-6
- Christopher, J., Davies, D. G., & Peter, K. J. (2010). Scalability of pseudospectral methods for geodynamo simulations. *Concurrency and Computation: Practice and Experience*, 22, 685–701. https://doi.org/10.1002/cpe
- Cowling, T. G. (1933). The magnetic field of sunspots. Monthly Notices of the Royal Astronomical Society, 94(1), 39-48. https://doi.org/10.1093/mnras/94.1.39
- Davidson, P. A. (2013). Scaling laws for planetary dynamos. *Geophysical Journal International*, 195(1), 67–74. https://doi.org/10.1093/gji/ggt167
- Gillet, N., & Jones, C. A. (2006). The quasi-geostrophic model for rapidly rotating spherical convection outside the tangent cylinder. *Journal of Fluid Mechanics*, 554(1), 343. https://doi.org/10.1017/s0022112006009219
- Glatzmaier, G. A., & Roberts, P. H. (1995a). A three-dimensional convective dynamo solution with rotating and finitely conducting inner core and mantle. *Physics of the Earth and Planetary Interiors*, 91(1), 63–75. https://doi.org/10.1016/0031-9201(95)03049-3
- Glatzmaiers, G. A., & Roberts, P. H. (1995b). A three-dimensional self-consistent computer simulation of a geomagnetic field reversal. Nature, 377(6546), 203–209. https://doi.org/10.1038/377203a0
- Grote, E., Busse, F. H., & Tilgner, A. (2000). Effects of hyperdiffusivities on dynamo simulations. *Geophysical Research Letters*, 27(13), 2001–2004. https://doi.org/10.1029/1999GL011155
- Huguet, L., & Amit, H. (2012). Magnetic energy transfer at the top of the Earth's core. Geophysical Journal International, 190(2), 856–870. https://doi.org/10.1111/j.1365-246X.2012.05542.x
- Johnson, C. L., & Constable, C. G. (1998). Persistently anomalous Pacific geomagnetic fields. Geophysical Research Letters, 25(7), 1011–1014. https://doi.org/10.1029/98GL50666
- Jones, C. A. (2011). Planetary magnetic fields and fluid dynamos. Annual Review of Fluid Mechanics, 43, 583–614. https://doi.org/10.1146/annurev-fluid-122109-160727
- King, E. M., & Buffett, B. A. (2013). Flow speeds and length scales in geodynamo models: The role of viscosity. *Earth and Planetary Science Letters*, 371–372, 156–162. https://doi.org/10.1016/j.epsl.2013.04.001
- Kono, M., & Roberts, P. H. (2002). Recent geodynamo simulations and observations of the geomagnetic field. *Reviews of Geophysics*, 40(4), 1013. https://doi.org/10.1029/2000RG000102
- Kuang, W. (1999). Force balances and convective state in the earth's core. *Physics of the Earth and Planetary Interiors*, 116(1), 65–79. https://doi.org/10.1016/S0031-9201(99)00116-8
- Kuang, W., & Bloxham, J. (1997). An Earth-like numerical dynamo model. Nature, 389(6649), 371-374. https://doi.org/10.1038/38712
- Kuang, W., & Bloxham, J. (1999). Numerical modeling of magnetohydrodynamic convection in a rapidly rotating spherical shell: Weak and strong field dynamo action. *Journal of Computational Physics*, 153(1), 51–81. https://doi.org/10.1006/jcph.1999.6274
- Kuang, W., Chao, B. F., & Chen, J. (2017). Decadal polar motion of the earth excited by the convective outer core from geodynamo simulations. *Journal of Geophysical Research: Solid Earth*, 122, 8459–8473. https://doi.org/10.1002/2017JB014555
- Kuang, W., Jiang, W., & Wang, T. (2008). Sudden termination of Martian dynamo? Implications from subcritical dynamo simulations. Geophysical Research Letters, 35, L14204. https://doi.org/10.1029/2008GL034183
- Olson, P. (2007). Overview. In G. Schubert (Ed.), *Treatise on geophysics* (pp. 1–30). Amsterdam: Elsevier. https://doi.org/10.1016/B978-044452748-6.00125-5
- Olson, P., Christensen, U., & Glatzmaier, G. A. (1999). Numerical modeling of the geodynamo: Mechanisms of field generation and equilibration. *Journal of Geophysical Research*, 104(B5), 10383–10404. https://doi.org/10.1029/1999JB900013

DONG ET AL. 18 of 19



- Oruba, L., & Dormy, E. (2014). Predictive scaling laws for spherical rotating dynamos. *Geophysical Journal International*, 198(2), 828–847. https://doi.org/10.1093/gji/ggu159
- Roberts, P. H. (2007). Theory of the geodynamo. In G. Schubert (Ed.), Treatise on geophysics (pp. 67–105). Amsterdam: Elsevier. https://doi.org/10.1016/B978-044452748-6.00133-4
- Roberts, P. H., & Chandrasekhar, S. (1968). On the thermal instability of a rotating-fluid sphere containing heat sources. *Philosophical Transactions of the Royal Society of London—Series A: Mathematical and Physical Sciences*, 263(1136), 93–117. https://doi.org/10.1098/rsta.1968.0007
- Roberts, P. H., & King, E. M. (2013). On the genesis of the Earth's magnetism. Reports on Progress in Physics, 76(9), 096801. https://doi.org/10.1088/0034-4885/76/9/096801
- Sarson, G. R., Jones, C. A., & Longbottom, A. W. (1998). Convection driven geodynamo models of varying Ekman number. Geophysical & Astrophysical Fluid Dynamics, 88(1–4), 225–259. https://doi.org/10.1080/03091929808245475
- Schaeffer, N., Jault, D., Nataf, H.-C., & Fournier, A. (2017). Turbulent geodynamo simulations: A leap toward Earth's core. *Geophysical Journal International*, 211(1), 1–29. https://doi.org/10.1093/gji/ggx265
- Schwaiger, T., Gastine, T., & Aubert, J. (2019). Force balance in numerical geodynamo simulations: A systematic study. *Geophysical Journal International*, 219, S101–S114. https://doi.org/10.1093/gji/ggz192/5480467
- Simitev, R., & Busse, F. H. (2005). Prandtl-number dependence of convection-driven dynamos in rotating spherical fluid shells. *Journal of Fluid Mechanics*, 532, 365–388. https://doi.org/10.1017/s0022112005004398
- Soderlund, K. M., King, E. M., & Aurnou, J. M. (2012). The influence of magnetic fields in planetary dynamo models. *Earth and Planetary Science Letters*, 333–334, 9–20. https://doi.org/10.1016/j.epsl.2012.03.038
- Sreenivasan, B., Sahoo, S., & Dhama, G. (2014). The role of buoyancy in polarity reversals of the geodynamo. *Geophysical Journal International*, 199(3), 1698–1708. https://doi.org/10.1093/gji/ggu340
- Starchenko, S. V., & Jones, C. A. (2002). Typical velocities and magnetic field strengths in planetary interiors. *Icarus*, 157(2), 426–435. https://doi.org/10.1006/icar.2002.6842
- Taylor, J. B. (1963). The magneto-hydrodynamics of a rotating fluid and the earth's dynamo problem. *Proceedings of the Royal Society of London*, 274, 274–283. https://doi.org/10.1098/rspa.1963.0130
- Wang, T., Wei, Z., Jiang, W., Kuang, W., & Ma, S. (2013). Martian magnetic field properties before the termination of its core dynamo. Science China Earth Sciences, 56(8), 1452–1458. https://doi.org/10.1007/s11430-012-4510-4
- Wicht, J., & Sanchez, S. (2019). Advances in geodynamo modeling. Geophysical & Astrophysical Fluid Dynamics, 113(1–2), 2–50. https://doi.org/10.1080/03091929.2019.1597074
- Yadav, R. K., Gastine, T., Christensen, U. R., Duarte, L. D. V., & Reiners, A. (2015). Effect of shear and magnetic field on the heat-transfer efficiency of convection in rotating spherical shells. *Geophysical Journal International*, 204(2), 1120–1133. https://doi.org/10.1093/gji/gmy506
- Yadav, R. K., Gastine, T., Christensen, U. R., Wolk, S. J., & Poppenhaeger, K. (2016). Approaching a realistic force balance in geodynamo simulations. Proceedings of the National Academy of Sciences of the United States of America, 113(43), 12065–12070. https://doi.org/10.1073/pnas.1608998113
- Zhang, K., & Jones, C. A. (1997). The effect of hyperviscosity on geodynamo models. *Geophysical Research Letters*, 24(22), 2869–2872. https://doi.org/10.1029/97GL02955

DONG ET AL. 19 of 19